JOURNAL OF SPACECRAFT AND ROCKETS
Vol. 46, No. 2, March–April 2009

Bluntness Impact on Lift-to-Drag Ratio of Hypersonic Wedge Flow

Wilson F. N. Santos*
National Institute for Space Research, 12630-000 Cachoeira Paulista, Brazil

DOI: 10.2514/1.41387

A computational investigation was conducted on rarefied hypersonic flow past truncated wedges at incidence. Positive angle-of-attack effects on the aerodynamic surface quantities have been investigated by employing the direct simulation Monte Carlo method. The results highlight the sensitivity of the heat transfer coefficient, the total drag coefficient, the total lift coefficient, and the lift-to-drag ratio to changes not only on the angle of attack but also on the frontal-face thickness of the leading edges. Some significant differences between sharp and blunt leading edges were noted on the surface quantities. Interesting features observed in these surface properties showed that even small leading-edge thickness, compared with the freestream mean free path, still has important effects on high Mach number leading-edge flows. The analysis is important because it is impossible to achieve ideally sharp leading edges of airframes such as waveriders.

Nomenclature

C_d = drag coefficient, $2F_D/\rho_\infty V_\infty^2 H$
C_f = skin friction coefficient, $2\tau_w/\rho_\infty V_\infty^2$
C_h = heat transfer coefficient, $2q_w/\rho_\infty V_\infty^3$
C_l = lift coefficient, $2F_L/\rho_\infty V_\infty^2 H$
C_p = pressure coefficient, $2(p_w - p_\infty)/\rho_\infty V_\infty^2$
d = molecular diameter, m
F_D = drag force, N
F_L = lift force, N
H = body height at the base, m
Kn = Knudsen number, λ/l
L = body length, m
l = characteristic length, m
M = Mach number
m = molecular mass, kg
N = number flux, $\mathrm{m}^{-2}\mathrm{s}^{-1}$
n = number density, m^{-3}
N_f = dimensionless number flux, $N/n_\infty V_\infty$
p = pressure, $\mathrm{N/m}^2$
q = heat flux, $\mathrm{W/m}^2$
R = circular cylinder radius, m
Re = Reynolds number, $\rho V l/\mu$
S = dimensionless arc length, s/λ_∞
s = arc length, m
T = temperature, K
t = frontal-face thickness, m
V = velocity, m/s
X = mole fraction
x, y = Cartesian axes in physical space, m
α = angle of attack, deg
η = coordinate normal to body surface, m
θ = wedge half angle, deg
λ = mean free path, m
ξ = coordinate tangent to body surface, m
ρ = density, $\mathrm{kg/m}^3$
τ = shear stress, $\mathrm{N/m}^2$
ω = viscosity index

Subscripts

t = relative to frontal-face thickness
w = wall conditions
∞ = freestream conditions

I. Introduction

INTEREST in the development of various types of hypersonic vehicles has recently seen a resurgence. One type of vehicle that is promising for hypersonic flight is the waverider. A waverider, first conceived by Nonweiler [1], is a lifting body that is derived from a known analytical flowfield such as flow over a two-dimensional wedge or flow around a slender cone. A waverider is designed analytically with an infinitely sharp leading edge for shock-wave attachment. Because the shock wave is attached to the leading edge of the vehicle, the upper and lower surfaces of the vehicle can be designed separately. Furthermore, the shock wave acts as a barrier in order to prevent spillage of higher-pressure airflow from the lower side of the vehicle to the upper side, thus allowing the potential for a high lift-to-drag (L/D) ratio at a high Mach number.

Usually, it is extremely difficult to construct a perfectly sharp leading edge. Any manufacturing error results in a significant deviation from the design contour. Even with the most efficient and careful fabrication process, the leading edge will be several microns thick. Moreover, sharp edges are difficult to maintain because they are easily damaged. It is not only due to difficulties in manufacturing technology and in the strength of the material that ideally sharp leading edges on airframes are impossible to achieve in practice. At hypersonic flight speeds, the thin leading edges would inevitably melt away because of the high heating associated with sharp edges and the impossibility of bleeding off the large quantities of heat liberated in the flow gas adjacent to the leading edge of the body through the thin tips. Therefore, for practical hypersonic configurations, leading edges should be blunt for heat transfer, manufacturing, and handling concerns. Because a blunt leading edge promotes shock-wave standoff, practical leading edges will have shock detachment, making leading-edge blunting a major concern in the design and prediction of flowfield over hypersonic waveriders.

The sharp leading edges of waveriders are a dominant factor in their high L/D ratio compared with conventional aerospace designs. In this context, investigation of the effects of either aerodynamically sharp leading edges [2,3] or no sharp leading edges [4–10] becomes important in the design of waverider configurations. Based on recent interest in hypersonic waveriders being considered for high-altitude/

Presented as Paper 0615 at the 45th AIAA Aerospace Sciences Meeting, Reno, NV; received 3 October 2008; revision received 26 December 2008; accepted for publication 2 January 2009.

*Researcher, Combustion and Propulsion Laboratory. Member AIAA.

low-density applications [11–15], Santos [2] has investigated the effect of the leading-edge thickness on the flowfield structure and on the aerodynamic surface quantities over truncated wedges. The thickness effect was examined for a range of Knudsen numbers, based on the frontal-face thickness, covering from the transition flow regime to the free molecular flow regime. The emphasis of the study was to provide a critical analysis on maximum allowable geometric bluntness, dictated by either handling or manufacturing requirements, resulting in reduced departures from ideal aerodynamic performance of the vehicle. Thus, it would allow the blunted leading edge to more closely represent the original sharp leading-edge flowfield. Such analysis is also important when a comparison is to be made between experimental results at the immediate vicinity of the leading edge and the theoretical results, which generally assume a zero-thickness leading edge.

The purpose of the present account is to extend further the previous analysis [2] on truncated wedges by investigating the impact of the angle of attack on the flowfield structure. For a positive angle of attack, changes occur on flowfield properties and shock strength and, thus, on aerodynamic forces and heat transfer. Moreover, the knowledge of these properties at a 0-deg angle of attack is not sufficient to predict with certainty the flow characteristics over these shapes with incidence. The incidence rise causes an asymmetry in the flow patterns as the stagnation point moves from the axis to the lower windward side. Of particular interest in this analysis is the aerodynamic performance of the leading edges because blunt leading edges at incidence will allow leakage of the high-pressure lower surface flow into the upper surface region, causing a reduction in the lift and, consequently, a reduction in the L/D ratio. Therefore, the important question to be answered is how sharp is sharp [16]?

In an effort to obtain further insight into the nature of the aerodynamic surface quantities of truncated wedges under hypersonic transition flow conditions, the essential characteristics of the angle-of-attack effect on heat transfer, drag, lift, and the L/D ratio will be examined for positive angle of attack with 0, 5, 10, 15, and 20 deg of incidence.

Under hypersonic transition flow conditions, at very high speeds and high altitudes, the flow about a given aerodynamic configuration may be sufficiently rarefied to preclude the use of continuum assumptions but not large enough for the use of the free molecular theory. In such an intermediate or transition rarefied gas regime, the complete investigation of the flowfield structure would require the full formulation of kinetic theory. The governing equation in the transition flow regime is the transport Boltzmann equation [17]. Nevertheless, in order to circumvent the difficult of a direct solution of the Boltzmann equation, the direct simulation Monte Carlo (DSMC) method [18] has been the appropriate choice for problems involving flows of rarefied hypersonic aerothermodynamics.

II. Leading-Edge Geometry Definition

The geometry of the leading edges in this work is the same as that presented in the previous work [2]. The truncated wedges are modeled by assuming a sharp-edged wedge of half angle θ with a circular cylinder of radius R inscribed tangent to this sharp leading edge. The truncated wedges are also tangent to the sharp-edged wedge and the cylinder at the same common point. It was defined a leading-edge half angle of 10 deg, a circular cylinder diameter of 10^{-2} m, and frontal-face thickness t/λ_∞ of 0, 0.01, 0.1, and 1, where λ_∞ is the freestream mean free path. Figure 1 illustrates schematically this construction. It was assumed that the truncated wedges are infinitely long but only the length L is considered, because the wake region behind the truncated wedges is not of interest in this investigation.

III. Methodology

The DSMC method, pioneered by Bird [18], has become the standard technique for simulating low-density gas dynamics. For these flows, the computational fluid dynamics (CFD) methods that rely on continuum relations to compute the flowfield structure will not provide accurate results in the upper atmosphere, because the assumptions made in developing the differential equations, on which CFD methods are based, break down on rarefied conditions.

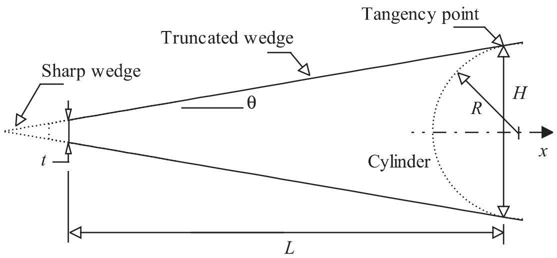

Fig. 1 Drawing illustrating the truncated wedges.

The DSMC method simulates real gas flows with various physical processes by means of a large number of modeling particles, each of which is a typical representative of a great number of real gas molecules. DSMC models the flow as being a collection of discrete particles, each one with a position, velocity, and internal energy. The state of particles is stored and modified with time as the particles move, collide, and undergo boundary interactions in simulated physical space. The simulation is always calculated as unsteady flow. However, a steady flow solution is obtained as the large time state of the simulation. Therefore, the DSMC method is basically an explicit time-marching algorithm.

Collisions in the present DSMC code are modeled by using the variable hard sphere molecular model [19] and the no time counter collision sampling technique [20]. Repartition of energy among internal and translational modes is controlled by the Borgnakke–Larsen statistical model [21]. Simulations are performed using a nonreacting gas model for a constant freestream gas composition consisting of 76.3% of N_2 and 23.7% of O_2. Energy exchanges between the translational and internal modes, such as rotation and vibration, are considered. Relaxation collision numbers of 5 and 50 were used for the calculations of rotation and vibration, respectively.

To easily account for particle–particle collisions, the physical space is divided into an arbitrary number of regions, which are subdivided into a certain number of computational cells. The cells are further subdivided into subcells. The physical space network is used to facilitate the choice of molecules for collisions and for the sampling of the macroscopic flow properties such as temperature, pressure, etc. In the DSMC algorithm, the linear dimensions of the cells should be small in comparison with the scale length of the macroscopic flow gradients normal to the streamwise directions, which means that the cell dimensions should be of the order of or smaller than the local mean free path [22,23]. The time step is set such that a typical molecule moves about one-third of the cell dimension at each time step. In addition, this time step is much less than the mean collision time [24,25], which is defined by the mean time between the successive collisions suffered by any particular molecule.

The computational domain used for the calculation is made large enough so that body disturbances do not reach the upstream and side boundaries, where freestream conditions are specified. A schematic view of the computational domain is depicted in Fig. 2. According to Fig. 2, side I is defined by the body surface. Diffuse reflection with complete surface thermal accommodation is the condition applied to this side. Side II is the freestream side through which simulated molecules enter and exit. Finally, the flow at the downstream outflow boundary, side III, is predominantly supersonic and vacuum condition is specified [26]. At this boundary, simulated molecules can only exit.

Application of a numerical method in order to solve practical problems requires a reliable way to estimate the accuracy of the solution. The numerical accuracy in DSMC method depends on the cell size chosen, on the time step as well as on the number of particles per computational cell. These effects were investigated in order to determine the number of cells and the number of particles required to achieve grid independence solutions.

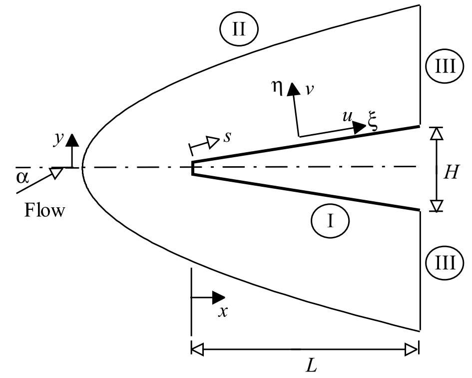

Fig. 2 Schematic view of the computational domain.

A grid independence study was made with three different structured meshes in each coordinate direction. The effect of altering the cell size in the ξ direction (see Fig. 2) was investigated with grids of 100 (coarse), 200 (standard), and 300 (fine) cells along the upper and lower surfaces, and 60 cells in the η direction for the bluntest leading edge investigated, $t/\lambda_\infty = 1$ case. In analogous fashion, an examination was made in the η direction with grids of 30 (coarse), 60 (standard), and 90 (fine) cells, and 200 cells in the ξ direction. From the total number of cells in the ξ direction, around 30% are located along the frontal surface and 70% distributed along the afterbody surface of the leading edges. In addition, each grid was made up of nonuniform cell spacing in both directions. The distribution can be controlled by a number of different distribution functions that allow the concentration of points in regions where high flow gradients or small mean free paths are expected. The effect (not shown) of changing the cell size in both directions on the heat transfer and pressure coefficients was rather insensitive to the range of cell spacing considered, indicating that the standard grid of 200×60 cells for the $t/\lambda_\infty = 1$ case is essentially grid independent. A similar procedure was performed for the other cases investigated.

IV. Flow Conditions

The freestream flow conditions used for the numerical simulation of flow past the leading edges are those given by Santos [2] and summarized in Table 1. The gas properties [18] are shown in Table 2.

The freestream velocity V_∞ is assumed to be constant at 3.56 km/s, which corresponds to a freestream Mach number M_∞ of 12. The translational and vibrational temperatures in the freestream are in equilibrium at 220 K, and the leading-edge surface has a constant wall temperature T_w of 880 K for all cases considered.

The overall Knudsen number Kn_t, defined as λ_∞/t, corresponds to ∞, 100, 10, and 1 for thickness t/λ_∞ of 0, 0.01, 0.1, and 1, respectively. Finally, the Reynolds number Re_t covers the range from 0.193 to 19.3, based on conditions in the undisturbed stream with frontal-face thickness t as the characteristic length.

Table 1 Freestream flow conditions

Parameter	Value
Altitude	70 km
Temperature, T_∞	220.0 K
Pressure, p_∞	5.582 N/m^2
Density, ρ_∞	8.753×10^{-5} kg/m^3
Viscosity, μ_∞	1.455×10^{-5} Ns/m^2
Number density, n_∞	1.8209×10^{21} m^{-3}
Mean free path, λ_∞	9.03×10^{-4} m

Table 2 Gas properties

	X	m, kg	d, m	ω
O_2	0.237	5.312×10^{-26}	4.01×10^{-10}	0.77
N_2	0.763	4.650×10^{-26}	4.11×10^{-10}	0.74

V. Computational Results and Discussion

To assess the overall performance of truncated wedges, this section will focus on the calculations of the aerodynamic surface quantities obtained from the DSMC results. Aerodynamic surface quantities of particular interest are number flux, heat transfer, pressure, skin friction, drag, lift, and the L/D ratio. Therefore, the purpose of this section is to discuss and to compare differences in the profiles of these properties, expressed in coefficient form, due to variations not only on the frontal-face thickness of the leading edges, but also on the angle of attack.

A. Number Flux

The number flux N is calculated by sampling the molecules impinging on the surface by unit time and unit area. A flux is regarded as positive if it is directed toward the body surface. The dependence of the number flux on the angle of attack α is shown in Figs. 3 and 4 for thickness Knudsen numbers Kn_t of 100 and 1, respectively. In this set of plots, distributions of the number flux are displayed separated along the frontal face, the leeward side, and the windward side of the leading edges. Also, N_f is the number flux N normalized by $n_\infty V_\infty$, S is the arc length s, normalized by the freestream mean free path λ_∞, measured from the shoulder of the leading edges, and Y is the height y along the frontal face also normalized by λ_∞. For convenience and later reference, the special case of a 0-deg angle of incidence, investigated previously by Santos [2], is also presented in these figures.

Referring to Figs. 3a–3c, it is observed that the number flux presents approximately a constant value along the frontal face for the angle-of-attack range investigated. As would be expected, for a positive angle of attack, the number flux along the afterbody surface in general decreases on leeward side, due to the flow expansion, and increases on windward side of the leading edge, due to the flow compression. Of particular interest in this set of plots is the distribution of the number flux along the frontal face, Fig. 3a. It is seen that the dimensionless number flux approaches the limit value $N/n_\infty V_\infty = 1$ predicted by the free molecular flow equations [18] for the case with 0-deg angle of incidence.

According to Figs. 4a–4c, it is noted that the number flux is high near the symmetry point ($Y = 0$) and decreases along the frontal face up to the frontal-face/afterbody junction with increasing the nose thickness (decreasing Kn_t). After that, it drops off sharply along the afterbody surface for the case with 0-deg angle of incidence, in contrast to the $Kn_t = 100$ case. Therefore, number flux to the front surface relies on the leading-edge thickness in that it increases with increasing the thickness t. One possible reason for this behavior may be related to the collisions of two groups of molecules, the molecules reflecting from the nose of the leading edge and the molecules oncoming from the freestream. The molecules that are reflected from the body surface, which have a lower kinetic energy, interact with the oncoming freestream molecules, which have a higher kinetic energy. As a result, the surface-reflected molecules recollide with the body surface, which produce an increase in the dimensionless number flux in this region. This behavior becomes important as the leading edge becomes blunt.

Interesting features may be recognized from this set of figures. In addition to the differences on the number flux along the frontal face, the number flux is significantly different on the afterbody surface for the cases shown. For the $Kn_t = 100$ case, the number flux is low at the frontal-face/afterbody junction and then increases to a peak value around a freestream mean free path downstream along the afterbody surface, around $S = 1$ for the case with 0-deg angle of incidence. Furthermore, the angle-of-attack effect is to move this peak value at stations $S > 1$ along both leeward side and windward side of the afterbody surface. In contrast, for the $Kn_t = 1$ case, the number flux presents the peak value at the frontal-face/afterbody junction for the case with 0-deg angle of incidence. Moreover, at incidence, no peak value is observed for the number flux along the leeward side of the afterbody surface. However, for angle of attack $\alpha > 15$ deg, the number flux increases above the value observed at the frontal-face/afterbody junction on the windward side of the afterbody surface. It should be mentioned in this context that the number flux distribution for the $Kn_t = 100$ case corresponds to a sharp or aerodynamically sharp leading edge, whereas the number flux distribution for the $Kn_t = 1$ case corresponds to a blunt leading edge.

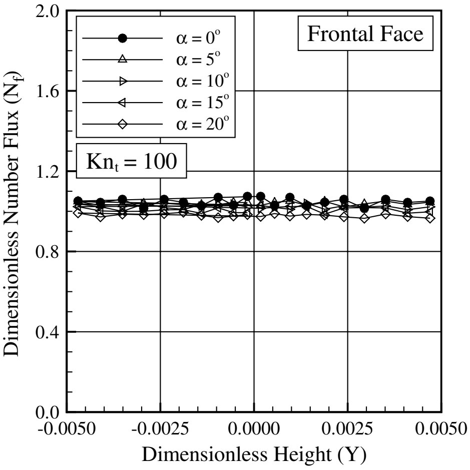

a) Frontal face

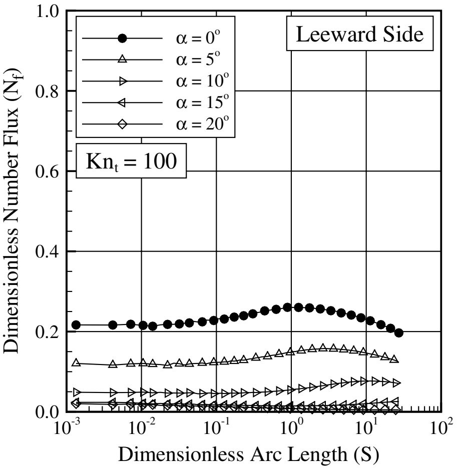

b) Leeward side

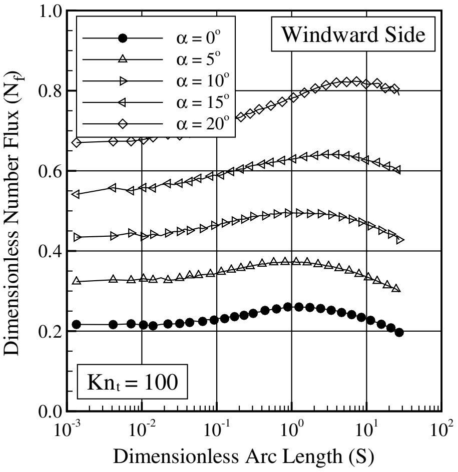

c) Windward side

Fig. 3 Dimensionless number flux N_f along the a) frontal face, b) leeward side, and c) windward side as a function of the angle of attack for a thickness Knudsen number Kn_t of 100.

B. Heat Transfer Coefficient

The heat flux q_w to the body surface is calculated by the net energy flux of the molecules impinging on the surface. The net heat flux q_w is related to the sum of the translational, rotational, and vibrational energies of both incident and reflected molecules. The heat flux is normalized by $\rho_\infty V_\infty^3/2$ and presented in terms of the heat transfer coefficient C_h.

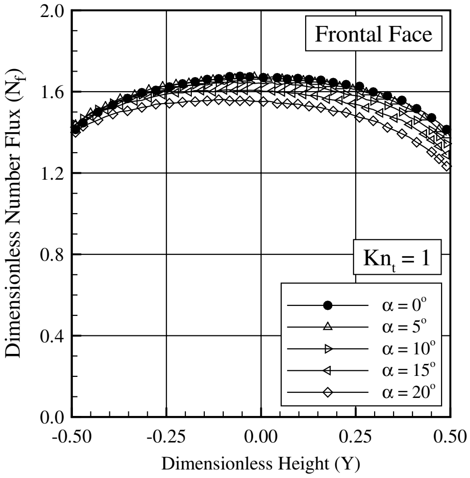

a) Frontal face

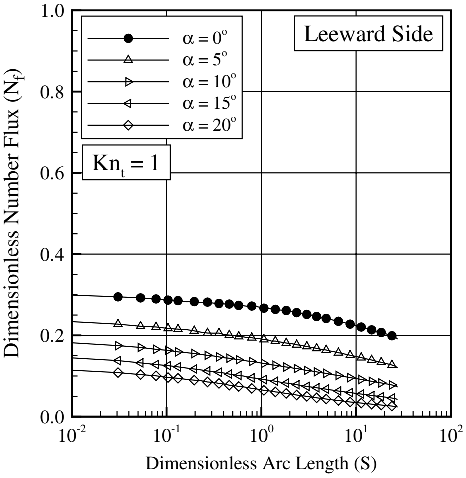

b) Leeward side

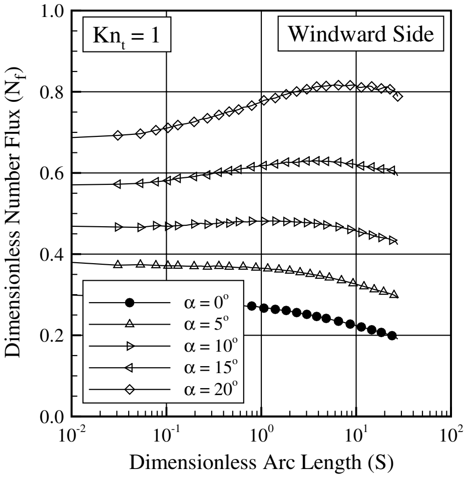

c)Windward side

Fig. 4 Dimensionless number flux N_f along the a) frontal face, b) leeward side, and (c) windward side as a function of the angle of attack for a thickness Knudsen number Kn_t of 1.

The heat flux q_w to the body surface was defined in terms of the incident and reflected flow properties and based upon the gas–surface interaction model of fully accommodated, complete diffuse reemission. The diffuse model assumes that the molecules are reflected equally in all directions, quite independently of their incident speed and direction. Because of the diffuse reflection model, the reflected thermal velocity of the molecules impinging on the surface is obtained from a Maxwellian distribution that takes into account the temperature of the body surface. In this fashion, as the wall temperature is the same for all the cases investigated, the number of molecules impinging on the surface plays the important role on the reflected contribution to the net heat flux to the body surface.

The angle-of-attack effect on heat transfer coefficient C_h is illustrated in Figs. 5 and 6 for thickness Knudsen numbers Kn_t of 100 and 1, respectively. It is seen from these figures that the heat transfer coefficient C_h is sensitive not only to the angle of attack but also to

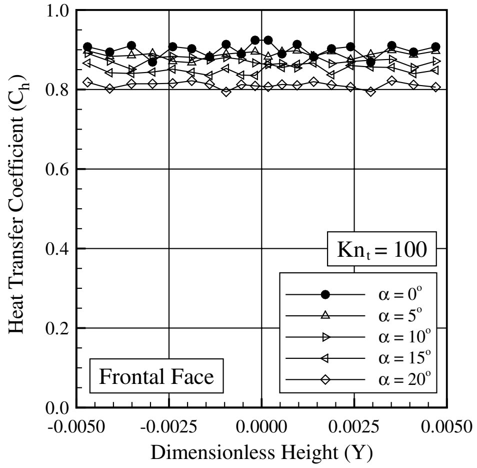

a) Frontal face

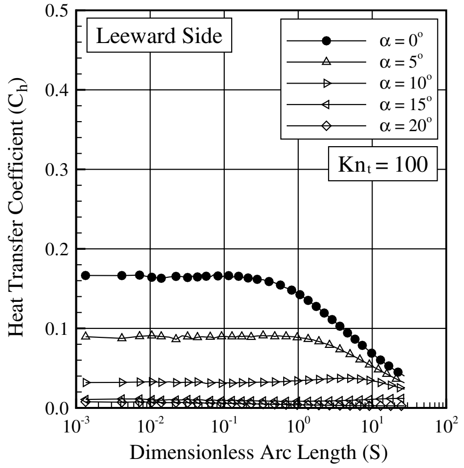

b) Leeward side

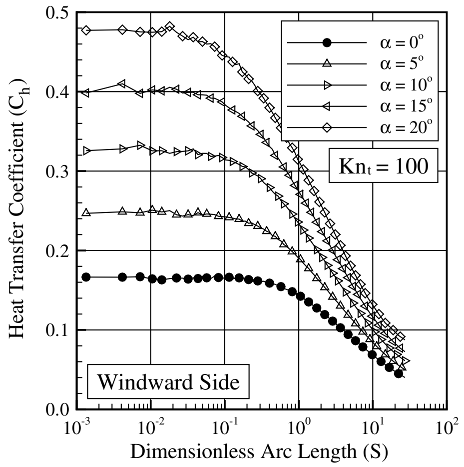

c) Windward side

Fig. 5 Heat transfer coefficient C_h along the a) frontal face, b) leeward side, and c) windward side as a function of the angle of attack for a thickness Knudsen number Kn_t of 100.

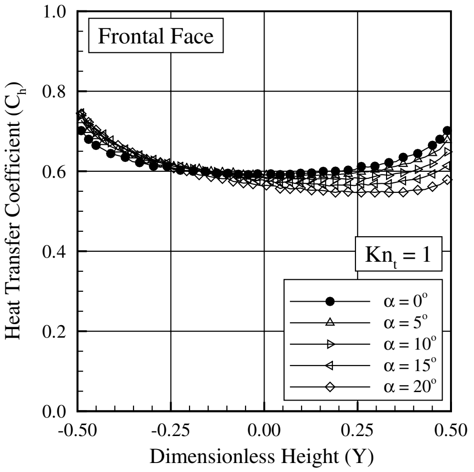

a) Frontal face

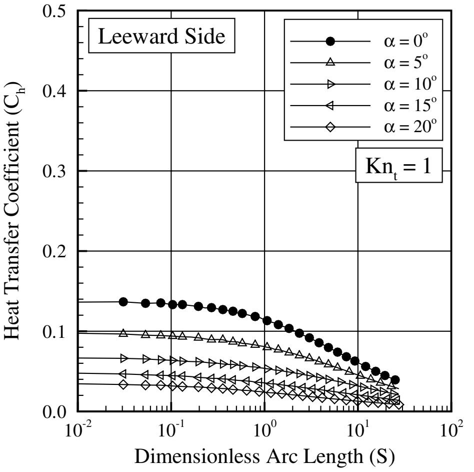

b) Leeward side

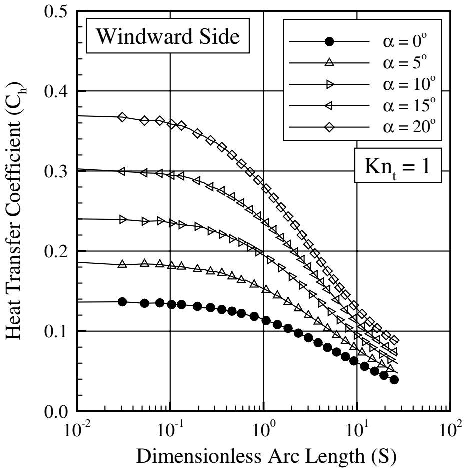

c) Windward side

Fig. 6 Heat transfer coefficient C_h along the a) frontal face, b) leeward side, and c) windward side as a function of the angle of attack for a thickness Knudsen number Kn_t of 1.

the frontal-face thickness. For the $Kn_t = 100$ case, the heat transfer coefficient remains essentially constant over the frontal surface. In contrast, for the bluntest case investigated, $Kn_t = 1$, C_h is low at the stagnation region and increases at the vicinity of the frontal-face/afterbody junction. It is clearly noticed that, along the afterbody surface, the heat transfer coefficient distribution presents a similar behavior on both leading edges in that it presents a constant value at the vicinity of the frontal-face/afterbody junction and then decreases sharply downstream along the body surface. The angle-of-attack effect on the heat transfer coefficient along the afterbody surface is similar for the flat-nose leading edges investigated in the sense that it decreases on the leeward side and increases on the windward side of the leading edges.

As would be expected, the blunter (flatter) the leading edge is, the lower the heat transfer coefficient at the stagnation point. Usually, the stagnation region is generally considered as being the most thermally stressed zone in sharp/blunt bodies, as shown by the $Kn_t = 100$ case. Nevertheless, as the frontal-face thickness increases, the most severe heat transfer region moves to the frontal-face/afterbody junction. As the number of molecules impinging on the frontal surface decreases at the vicinity of the frontal-face/afterbody junction (see Fig. 4), then the velocity of the molecules increases as the flow approaches the junction of the leading edge, thus, increasing the heat transfer coefficient. Moreover, the contribution of the translational energy to the net heat flux varies with the square of the velocity of the molecules.

For comparison purpose, the heat transfer coefficient at the stagnation point predicted by the free molecular equations [18] is $C_{ho} = 0.912$ for the case with 0-deg angle of incidence. According to Fig. 5, the stagnation point heating tends to this limit value as the leading edge becomes sharp, that is, by reducing the nose thickness of the leading edges (increasing Kn_t).

C. Pressure Coefficient

The pressure p_w on the body surface is calculated by the sum of the normal momentum fluxes of both incident and reflected molecules at each time step. Results are presented in terms of the pressure coefficient C_p.

Variations of the pressure coefficient C_p caused by changes on the angle of attack as well as on the leading-edge thickness are demonstrated in Figs. 7 and 8 for thickness Knudsen numbers Kn_t of 100 and 1, respectively. It can be noted from this set of diagrams that the pressure coefficient is high along the frontal surface, basically a constant value along it, and decreases dramatically transitioning from the frontal surface to the afterbody surface around the sharp shoulder. This effect is more pronounced with a decreasing Knudsen number Kn_t, that is, as the nose becomes flatter. Along the afterbody surface, the pressure coefficient follows the trend presented by the number flux distribution (Figs. 4 and 5); it decreases along the leeward side and increases on the windward side of the body surface with the angle-of-attack rise. As expected, blunting the leading edge causes the shock wave to be detached further than that of a sharp leading edge, resulting in the spillage of the high-pressure gas from the underside to the top surface. As a result, the gas leakage causes an increase in the pressure acting on the upper surface, thereby reducing the lift force as will be seen subsequently.

As a base of comparison, the pressure coefficient C_p predicted by the free molecular flow equations on the frontal-face surface is 2.35 for the case with 0-deg angle of incidence. Therefore, for the thinnest flat leading edge investigated $t/\lambda_\infty = 0.01$, which corresponds to $Kn_t = 100$, the flow seems to approach the free collision flow along the frontal face for a small angle of attack (as shown in Fig. 7a) as was pointed out earlier.

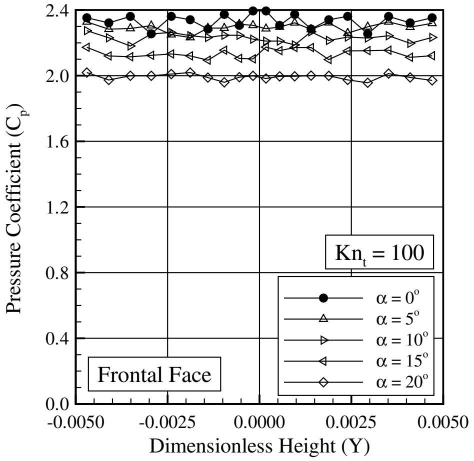

a) Frontal face

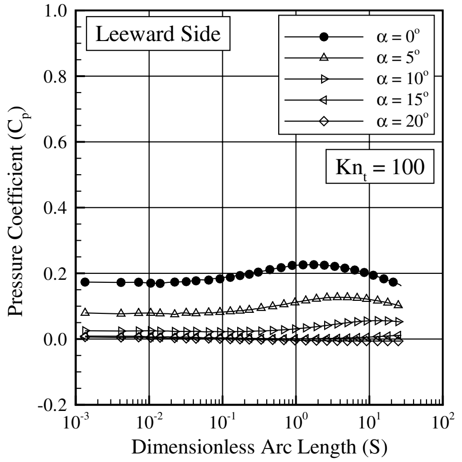

b) Leeward side

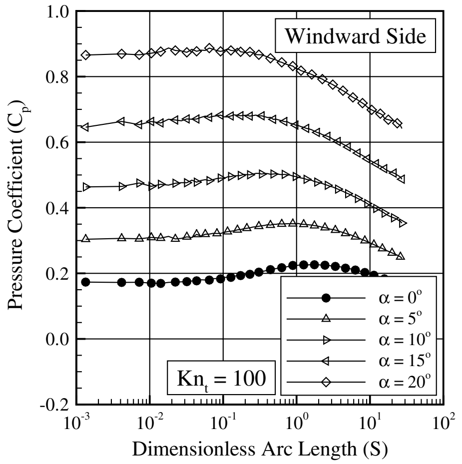

c) Windward side

Fig. 7 Pressure coefficient C_p along the a) frontal face, b) leeward side, and c) windward side as a function of the angle of attack for a thickness Knudsen number Kn_t of 100.

D. Skin Friction Coefficient

The shear stress τ_w on the body surface is calculated by averaging the tangential momentum transfer of the molecules impinging on the surface. For the diffuse reflection model imposed for the gas–surface interaction, reflected molecules have a tangential moment equal to zero, because the molecules essentially lose, on average, their tangential velocity component. The shear stress τ_w on the body surface is normalized by $\rho_\infty V_\infty^2/2$ and presented in terms of the dimensionless skin friction coefficient C_f.

The influence of the leading-edge nose thickness and the angle of attack on the skin friction coefficient is displayed in Figs. 9 and 10 for thickness Knudsen numbers Kn_t of 100 and 1, respectively. According to these figures, interesting characteristics on the skin friction coefficient C_f are observed on the frontal face of the leading edges. For the $Kn_t = 100$ case, the skin friction coefficient is

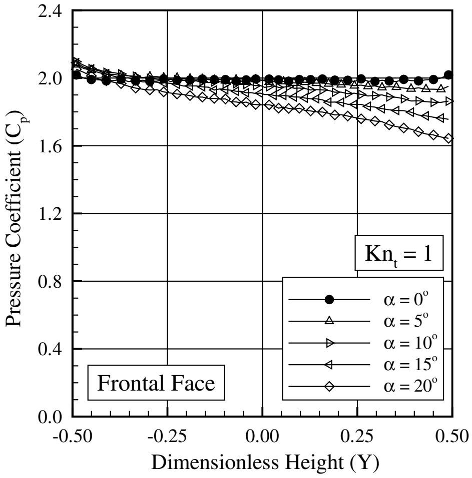

a) Frontal face

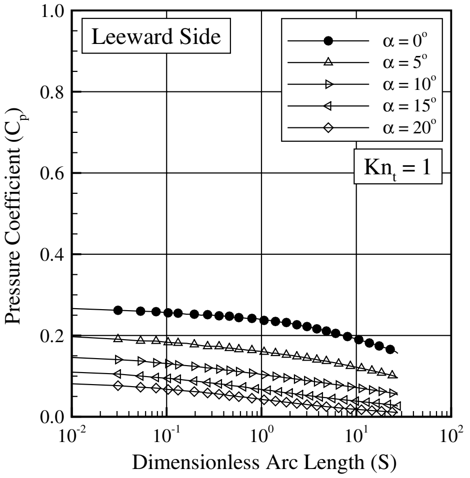

b) Leeward side

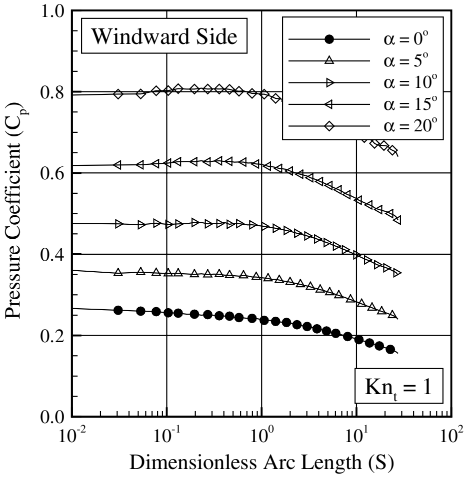

c) Windward side

Fig. 8 Pressure coefficient C_p along the a) frontal face, b) leeward side, and c) windward side as a function of the angle of attack for a thickness Knudsen number Kn_t of 1.

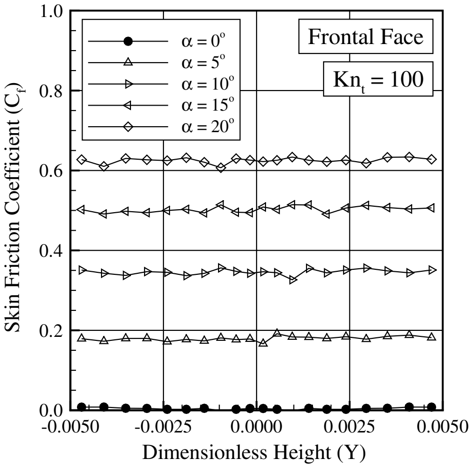

a) Frontal face

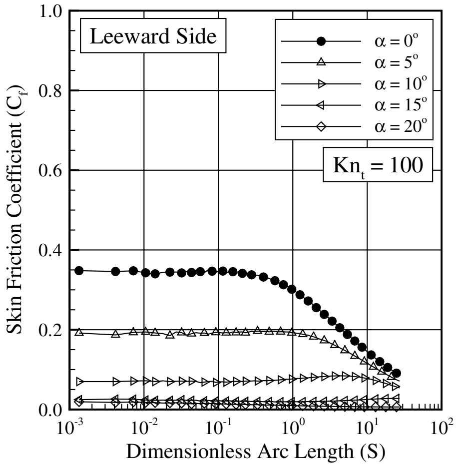

b) Leeward side

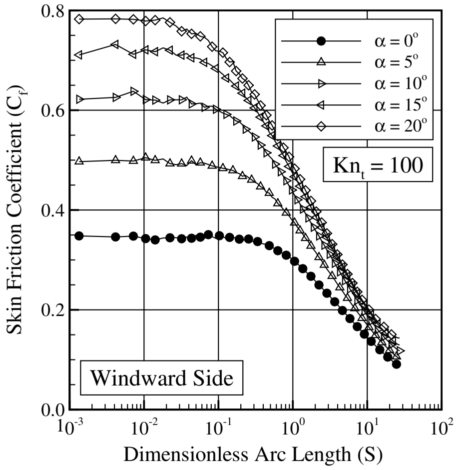

c) Windward side

Fig. 9 Skin friction coefficient C_f along the a) frontal face, b) leeward side, and c) windward side as a function of the angle of attack for a thickness Knudsen number Kn_t of 100.

constant along the flat face. In addition, the constant value trend is preserved with increasing the incidence. Conversely, for the $Kn_t = 1$ case at incidence, the skin friction coefficient increases from a minimum value at the frontal-face/afterbody junction on the windward side up to a maximum value at the frontal-face/afterbody junction on the leeward side of the leading edges. It is also noted that, along the afterbody surface, the distribution for the skin friction coefficient C_f is preserved, as compared with the case of 0-deg angle of incidence, in that it presents a constant value at the vicinity of the frontal-face/afterbody junction and then decreases downstream along the body surface. The angle-of-attack effect on the skin friction coefficient along the afterbody surface is similar to the pressure coefficient for the leading edges investigated in the sense that it decreases on the leeward side and increases on the windward side of the leading edges.

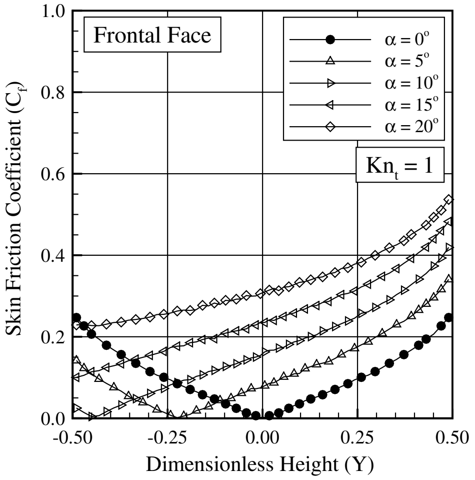

a) Frontal face

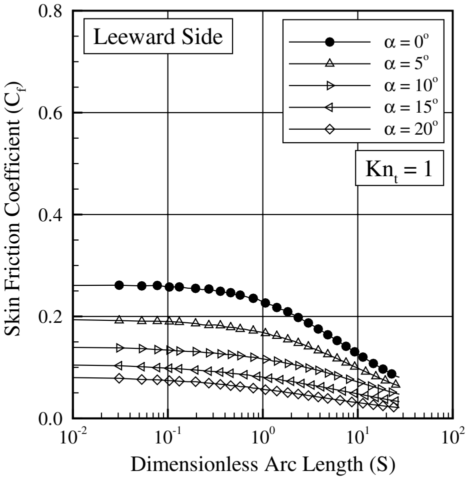

b) Leeward side

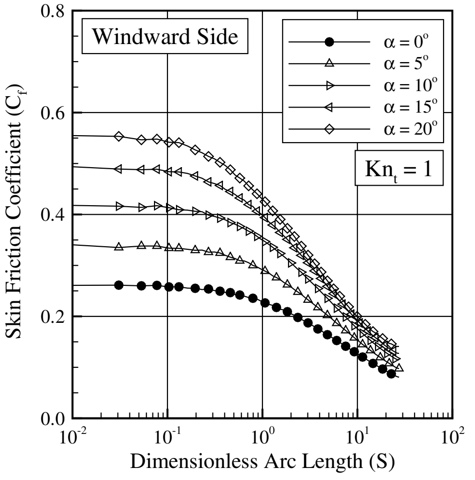

c) Windward side

Fig. 10 Skin friction coefficient C_f along the a) frontal face, b) leeward side, and c) windward side as a function of the angle of attack for a thickness Knudsen number Kn_t of 1.

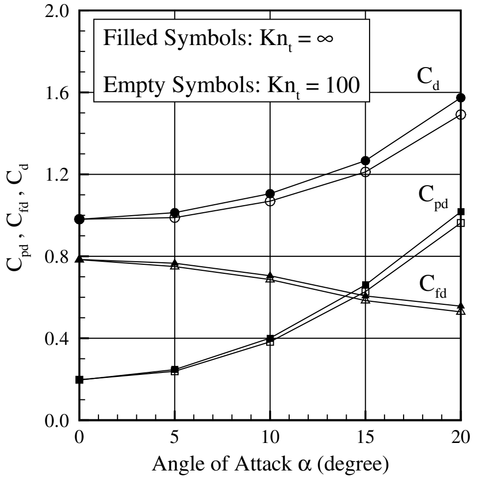

a) Kn_t =100

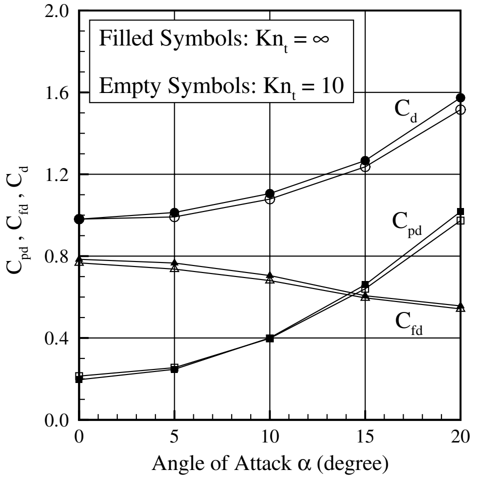

b) Kn_t =10

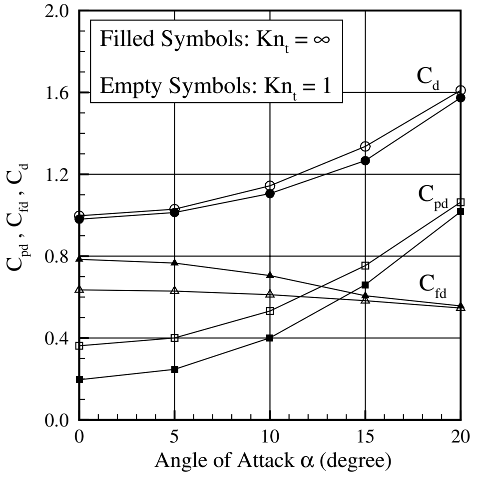

c) Kn_t =1

Fig. 11 Pressure drag C_{pd}, skin friction drag C_{fd}, and total drag C_d coefficients as a function of the angle of attack for thickness Knudsen numbers Kn_t of a) 100, b) 10, and c) 1.

E. Total Drag Coefficient

The drag on a surface in a gas flow results from the interchange of momentum between the surface and the molecules colliding with the surface. The total drag is obtained by the integration of the pressure p_w and shear stress τ_w distributions in the flow direction from the stagnation point of the leading edge to the station L that corresponds to the tangent point common to all the leading edges (see Fig. 1). It is important to mention that the values for the total drag were obtained by assuming the shapes acting as leading edges. Therefore, no base pressure effects were taken into account on the calculations. Results for total drag are normalized by $\rho_\infty V_\infty^2 H/2$ and presented as the total drag coefficient C_d and its components of the pressure drag coefficient C_{pd} and the skin friction drag coefficient C_{fd}.

The impact of the leading-edge bluntness and of the angle of attack on the total drag coefficient C_d is demonstrated in Figs. 11a–11c for

Table 3 Total drag coefficient C_d for the leading edges as a function of the angle of attack α

α	$Kn_t = \infty$	$Kn_t = 100$	$Kn_t = 10$	$Kn_t = 1$
0 deg	0.980	0.981	0.981	0.997
5 deg	1.013	0.989	0.991	1.029
10 deg	1.106	1.069	1.079	1.144
15 deg	1.267	1.212	1.236	1.336
20 deg	1.574	1.492	1.516	1.610

thickness Knudsen numbers Kn_t of 100, 10, and 1, respectively. In this group of plots, the pressure drag C_{pd}, skin friction drag C_{fd}, and total drag C_d for flat-face leading edges are compared with the sharp leading-edge case. Therefore, full symbols stand for sharp leading edge $Kn_t = \infty$, and empty symbols for flat-face leading edges Kn_t of 100, 10 or 1. For completeness, the results for total drag coefficient are tabulated in Table 3.

Interesting features may be seen in Figs. 11a–11c as well as in Table 3. By considering the cases with a 0-deg angle of incidence, it is clearly noticed that the major contribution to the total drag C_d is given by the skin friction drag C_{fd}. As the leading edge becomes blunter, the contribution of the pressure drag C_{pd} to the total drag increases and the contribution of the skin friction drag C_{fd} decreases. As a result of these two opposite behaviors, no appreciable changes are observed in the total drag coefficient for the nose thicknesses investigated. On the other hand, as would be expected, appreciable changes are observed in the total drag coefficient C_d with the angle-of-attack rise. By increasing the angle of attack, the leading edges are seen from the freestream as blunt bodies. Consequently, the contribution of the pressure drag C_{pd} to the total drag C_d increases significantly whereas the skin friction drag contribution slightly decreases. A balance on these two contributions is observed for the cases with a 15-deg angle of incidence.

F. Total Lift Coefficient

The lift force is obtained by the integration of the pressure p_w and shear stress τ_w distributions from the stagnation point of the leading edge to the station L in the normal direction of the flow. Results for total lift are normalized by $\rho_\infty V_\infty^2 H/2$ and presented as the total lift coefficient C_l and its components of the pressure lift coefficient C_{pl} and the skin friction lift coefficient C_{fl}.

The extent of changes on total lift coefficient C_l due to variation on the leading-edge thickness and on the angle of attack is illustrated in Figs. 12a–12c for thickness Knudsen numbers Kn_t of 100, 10, and 1, respectively. In a similar way, in this set of diagrams, full symbols stand for sharp leading edge $Kn_t = \infty$ and empty symbols for flat-face leading edges Kn_t of 100, 10, or 1. For convenience, Table 4 tabulates the total lift coefficient for all of the leading edges investigated.

Referring to Figs. 12a–12c and Table 4, it is clearly noticed that appreciable changes occur in the total lift coefficient C_l by introducing the frontal face into the leading edges. As a base of comparison, the total lift coefficient for leading-edge thicknesses t/λ_∞ of 0.01, 0.1, and 1, which correspond to a Kn_t of 100, 10, and 1, with a 5-deg angle of incidence, is reduced by 8.8, 9.6, and 20.1%, respectively, as compared with that for the zero-thickness leading edge $Kn_t = \infty$. On the other hand, for a 20-deg angle of incidence, the reduction on the total lift coefficient C_l for a Kn_t of 100, 10, and 1 is around 5.6, 7.1, and 18.1%, respectively, as compared with the zero-thickness leading-edge $Kn_t = \infty$, at the same angle of incidence. Consequently, even a small flat face of 100th of the freestream mean free path λ_∞ results in an appreciable reduction in the total lift coefficient.

Table 4 Total lift coefficient C_l for the leading edges as a function of the angle of attack α.

α	$Kn_t = \infty$	$Kn_t = 100$	$Kn_t = 10$	$Kn_t = 1$
5 deg	0.364	0.332	0.329	0.291
10 deg	0.740	0.692	0.682	0.588
15 deg	1.121	1.057	1.033	0.888
20 deg	1.440	1.359	1.338	1.180

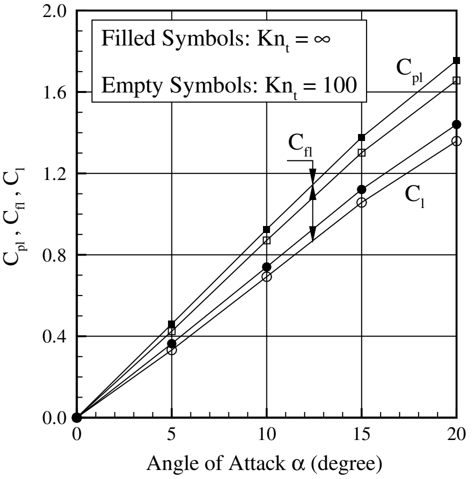

a) Kn_t =100

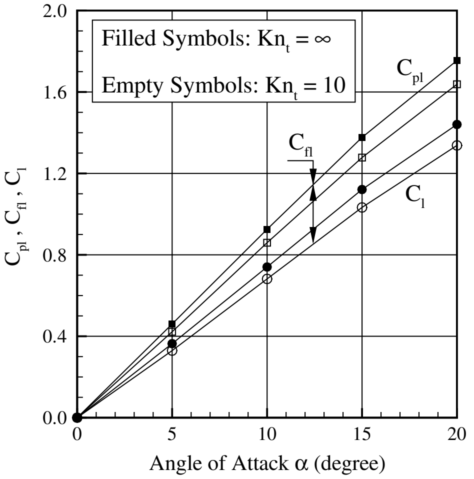

b) Kn_t =10

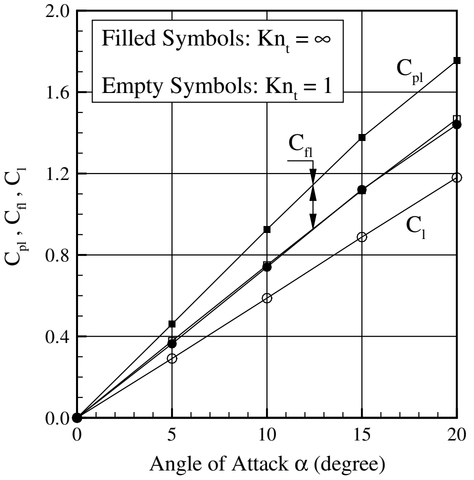

c) Kn_t =1

Fig. 12 Pressure lift C_{pl}, skin friction lift C_{fl}, and total lift C_l coefficients as a function of the angle of attack for thickness Knudsen numbers Kn_t of a) 100, b) 10, and c) 1.

In what follows, it becomes instructive to consider the L/D ratio. The L/D ratio is displayed in Fig. 13 as a function of the angle of attack α for the leading edges investigated. Also, the results are

Table 5 L/D ratio for the leading edges as a function of the angle of attack α

α	$Kn_t = \infty$	$Kn_t = 100$	$Kn_t = 10$	$Kn_t = 1$
5 deg	0.359	0.336	0.332	0.283
10 deg	0.669	0.648	0.632	0.514
15 deg	0.885	0.872	0.835	0.665
20 deg	0.915	0.911	0.883	0.733

tabulated in Table 5. According to Table 5, for a 5-deg angle of incidence, the L/D ratio for leading-edge thickness corresponding to a Kn_t of 100, 10, and 1 is reduced approximately by 6.4, 7.5, and 21.1%, respectively, as compared with that for zero-thickness leading edge $Kn_t = \infty$. For a 20-deg angle of incidence, the reduction on the L/D ratio for a Kn_t of 100, 10, and 1 is around 0.4, 3.5, and 19.9%, respectively, as compared with the zero-thickness leading edge $Kn_t = \infty$, at the same angle of incidence. Thus, effects of prescribed leading-edge truncation are established from the results of the L/D ratio or lift coefficient C_l.

VI. Conclusions

Computations of a rarefied hypersonic flow on sharp/blunt leading edges have been performed by using the direct simulation Monte Carlo method. The calculations provided information concerning the nature of the aerodynamic surface quantities for a family of truncated wedges.

Angle-of-attack effects on pressure, skin friction, heat transfer, and drag and lift coefficients for a wide range of parameters were investigated. The incidence ranged from 0 to 20 deg. In addition, the leading-edge thickness ranged from 0.01 to 1 of the freestream mean free path, corresponding thickness Knudsen numbers from 100 to 1. Cases considered in this study covered the hypersonic flow from the transitional flow regime to the free molecular flow regime.

The analysis showed that the total drag coefficient slightly decreased for the "aerodynamically sharp" leading edges investigated, that is, leading-edge thicknesses of 100th and one-tenth of the freestream mean free path, and increased for the "blunt" leading-edge case, leading-edge thickness with one freestream mean free path. Nevertheless, at incidence, a significant increase in the total drag coefficient was observed as compared with that with 0-deg angle of incidence. However, the same trend for the total drag was observed for aerodynamically sharp and blunt leading edges. In addition, it was found that the lift coefficient decreased by increasing the frontal face of the leading edges. Moreover, the analysis verified that even the smaller leading-edge bluntness resulted in significant reduction on the lift-to-drag ratio.

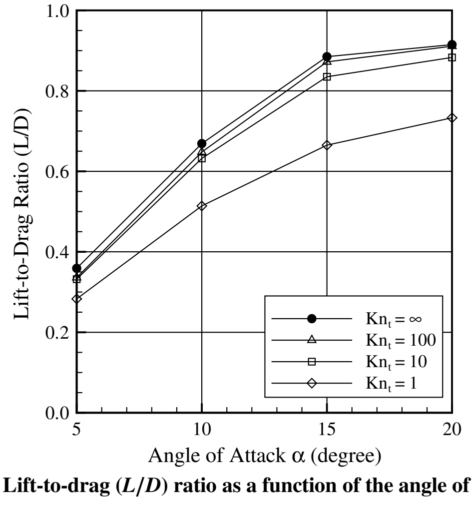

Fig. 13 Lift-to-drag (L/D) ratio as a function of the angle of attack α.

References

[1] Nonweiler, T. R. F., "Aerodynamic Problems of Manned Space Vehicles," *Journal of the Royal Aeronautical Society*, Vol. 63, Sept. 1959, pp. 521–528.

[2] Santos, W. F. N., "Flat-Faced Leading-Edge Effects in Low-Density Hypersonic Wedge Flow," *Journal of Spacecraft and Rockets*, Vol. 42, No. 1, 2005, pp. 22–29. doi:10.2514/1.4907

[3] Santos, W. F. N., "Effects of Compressibility on Aerodynamic Surface Quantities over Low-Density Hypersonic Wedge Flow," *Journal of the Brazilian Society of Mechanical Sciences and Engineering*, Vol. 28, No. 3, 2006, pp. 362–372.doi:10.1590/S1678-58782006000300015

[4] Gillum, M. J., and Lewis, M. J., "Experimental Results on a Mach 14 Waverider with Blunt Leading Edges," *Journal of Aircraft*, Vol. 34, No. 3, 1997, p. 296. doi:10.2514/2.2198

[5] O'Brien, T. F., and Lewis, M. J., "Power Law Shapes for Leading-Edge Blunting with Minimal Shock Standoff," *Journal of Spacecraft and Rockets*, Vol. 36, No. 5, 1999, pp. 653–658. doi:10.2514/2.3497

[6] Mazhul, I. I., and Rackchimov, R. D., "Hypersonic Power-Law Shaped Waveriders in Off-Design Regimes," *Journal of Aircraft*, Vol. 41, No. 4, 2004, pp. 839–845. doi:10.2514/1.386

[7] Santos, W. F. N., and Lewis, M. J., "Power Law Shaped Leading Edges in Rarefied Hypersonic Flow," *Journal of Spacecraft and Rockets*, Vol. 39, No. 6, 2002, pp. 917–925. doi:10.2514/2.3899

[8] Santos, W. F. N., and Lewis, M. J., "Calculation of Shock Wave Structure over Power Law Bodies in Hypersonic Flow," *Journal of Spacecraft and Rockets*, Vol. 42, No. 2, 2005, pp. 213–222. doi:10.2514/1.5635

[9] Santos, W. F. N., and Lewis, M. J., "Aerothermodynamic Performance Analysis of Hypersonic Flow on Power Law Leading Edges," *Journal of Spacecraft and Rockets*, Vol. 42, No. 4, 2005, pp. 588–597. doi:10.2514/1.9550

[10] Santos, W. F. N., "Some Physical and Computational Aspects of Shock Wave over Power-law Leading Edges," *Physics of Fluids*, Vol. 20, No. 1, 2008, pp. 016101–11.doi:10.1063/1.2831135

[11] Anderson, J. L., "Tethered Aerothermodynamic Research for Hypersonic Waveriders," *Proceedings of the 1st International Hypersonic Waverider Symposium*, Univ. of Maryland, College Park, MD, 1990.

[12] Potter, J. L., and Rockaway, J. K., "Aerodynamic Optimization for Hypersonic Flight at Very High Altitudes," *Rarefied Gas Dynamics: Space Science and Engineering*, edited by B. D. Shizgal and D. P. Weaver, Progress in Astronautics and Aeronautics, AIAA, New York, Vol. 160, 1994, pp. 296–307.

[13] Rault, D. F. G., "Aerodynamic Characteristics of a Hypersonic Viscous Optimized Waverider at High Altitude," *Journal of Spacecraft and Rockets*, Vol. 31, No. 5, 1994, pp. 719–727. doi:10.2514/3.26504

[14] Graves, R. E., and Argrow, B. M., "Aerodynamic Performance of an Osculating-Cones Waverider at High Altitudes," *35th AIAA Thermophysics Conference, Anaheim, CA*, AIAA Paper 2001-2960, 2001.

[15] Shvets, A. I., Voronin, V. I., Blankson, I. M., Khikine, V., and Thomas, L., "On Waverider Performance with Hypersonic Flight Speed and High Altitudes," *43rd AIAA Aerospace Sciences Meeting and Exhibit, Reno, NV*, AIAA Paper 2005-0512, 2005.

[16] Mason, W. H., and Lee, J., "Aerodynamically Blunt and Sharp Bodies," *Journal of Spacecraft and Rockets*, Vol. 31, No. 3, 1994, pp. 378–382. doi:10.2514/3.26449

[17] Cercignani, C., *The Boltzmann Equation and Its Applications*, Springer–Verlag, New York, 1988.

[18] Bird, G. A., *Molecular Gas Dynamics and the Direct Simulation of Gas Flows*, Oxford Univ. Press, Oxford, England, UK, 1994.

[19] Bird, G. A., "Monte Carlo Simulation in an Engineering Context," *Progress in Astronautics and Aeronautics: Rarefied Gas Dynamics*, edited by S. S. Fisher, Vol. 74, No. 1, AIAA, New York, 1981, pp. 239–255.

[20] Bird, G. A., "Perception of Numerical Method in Rarefied Gasdynamics," *Rarefied Gas Dynamics: Theoretical and Computational Techniques*," edited by E. P. Muntz, D. P. Weaver, and D. H. Capbell, Vol. 118, Progress in Astronautics and Aeronautics, AIAA, New York, 1989, pp. 374–395.

[21] Borgnakke, C., and Larsen, P. S., "Statistical Collision Model for Monte Carlo Simulation of Polyatomic Gas Mixture," *Journal of*

Computational Physics, Vol. 18, No. 4, 1975, pp. 405–420. doi:10.1016/0021-9991(75)90094-7

[22] Alexander, F. J., Garcia, A. L., and Alder, B. J., “Cell Size Dependence of Transport Coefficient in Stochastic Particle Algorithms,” *Physics of Fluids*, Vol. 10, No. 6, 1998, pp. 1540–1542. doi:10.1063/1.869674

[23] Alexander, F. J., Garcia, A. L., and Alder, B. J., “Erratum: Cell Size Dependence of Transport Coefficient is Stochastic Particle Algorithms,” *Physics of Fluids*, Vol. 12, No. 3, 2000, pp. 731–731. doi:10.1063/1.870278

[24] Garcia, A. L., and Wagner, W., “Time Step Truncation Error in Direct Simulation Monte Carlo,” *Physics of Fluids*, Vol. 12, No. 10, 2000, pp. 2621–2633. doi:10.1063/1.1289691

[25] Hadjiconstantinou, N. G., “Analysis of Discretization in the Direct Simulation Monte Carlo,” *Physics of Fluids*, Vol. 12, No. 10, 2000, pp. 2634–2638. doi:10.1063/1.1289393

[26] Guo, K., and Liaw, G.-S., “A Review: Boundary Conditions for the DSMC Method,” *35th AIAA Thermophysics Conference, Anaheim, CA*, AIAA Paper 2001-953, 2001.

I. Boyd
Associate Editor